J. Fluid Mech. (2009), *vol.* 625, *pp.* 445–474.
doi:10.1017/S0022112008005685 Printed in the United Kingdom

Hydrodynamic propulsion of human sperm

ERIC A. GILLIES[1], RICHARD M. CANNON[1], RICHARD B. GREEN[1] AND ALLAN A. PACEY[2]†

[1]Department of Aerospace Engineering, University of Glasgow, Glasgow G12 8QQ, UK

[2]Academic Unit of Reproductive and Developmental Medicine, School of Medicine and Biomedical Sciences, University of Sheffield, Sheffield S10 2SF, UK

(Received 19 February 2008 and in revised form 15 December 2008)

The detailed fluid mechanics of sperm propulsion are fundamental to our understanding of reproduction. In this paper, we aim to model a human sperm swimming in a microscope slide chamber. We model the sperm itself by a distribution of regularized stokeslets over an ellipsoidal sperm head and along an infinitesimally thin flagellum. The slide chamber walls are modelled as parallel plates, also discretized by a distribution of regularized stokeslets. The sperm flagellar motion, used in our model, is obtained by digital microscopy of human sperm swimming in slide chambers. We compare the results of our simulation with previous numerical studies of flagellar propulsion, and compare our computations of sperm kinematics with those of the actual sperm measured by digital microscopy. We find that there is an excellent quantitative match of transverse and angular velocities between our simulations and experimental measurements of sperm. We also find a good qualitative match of longitudinal velocities and computed tracks with those measured in our experiment. Our computations of average sperm power consumption fall within the range obtained by other authors. We use the hydrodynamic model, and a prototype flagellar motion derived from experiment, as a predictive tool, and investigate how sperm kinematics are affected by changes to head morphology, as human sperm have large variability in head size and shape. Results are shown which indicate the increase in predicted straight-line velocity of the sperm as the head width is reduced and the increase in lateral movement as the head length is reduced. Predicted power consumption, however, shows a minimum close to the normal head aspect ratio.

1. Introduction

An understanding of the fluid mechanics of sperm propulsion is fundamental to our understanding of the biology of reproduction (Fauci & Dillon 2006). This fluid flow may be approximated by the inertialess Stokes equations (Gray & Hancock 1955), where the cell is propelled by zero-thrust swimming (Lighthill 1976).

Many previous studies of flagellar propulsion have used spermatozoa as an archetype. Taylor (1951) began the first quantitative analyses of swimming micro-organisms by assuming the flagellum as a two-dimensional, small amplitude sheet. More realistic geometries, including models with high amplitude, thin flagella, were developed by Hancock (1953), who placed a distribution of stokeslets and doublets, singular solutions to the Stokes equations, along the flagellum centreline. This

† Email address for correspondence: e.gillies@aero.gla.ac.uk

slender-body theory (SBT) approach did not account for a head attached to the flagellum. Gray & Hancock (1955) introduced resistive-force theory (RFT) where tangential and normal resistance coefficients, C_t and C_n, proportional to the relative velocity of an element of the flagellum, are derived using SBT for a given flagellar wave and thickness. Integration of these coefficients gives a flagellar propulsive force and moment that, when taken in conjunction with cell tangential and normal drag, allow calculation of the propulsive velocity of the cell. This early model was used by many researchers in studying sperm propulsion (see Brennen & Winet 1977). Brokaw (1970) used RFT to analyse arbitrary planar motions of a sperm tail and compared computed average propulsive velocities with those found in experiment. Brokaw (1970) was perhaps the first to suggest using a series of photographs of cell position and flagellar motion to compare computed cell trajectories with experiment. Yundt, Shack & Lardner (1975) carried out this suggestion by taking high-speed cinematography of sea urchin, rabbit, and bull sperm, and used Brokaw's modified RFT to compute sperm tracks resulting from the observed tail motions. These computed tracks were compared to the observed tracks. The approach of Yundt *et al.* (1975) is the one we update here using digital image processing and a stokeslet simulation. These SBT and RFT approaches have been thoroughly reviewed by Lighthill (1976) and Brennen & Winet (1977), and compared by Johnson & Brokaw (1979). Higdon (1979) developed an improved SBT incorporating an image system of the flagellum inside a spherical cell head – this exact approach accounted for the hydrodynamic interaction between head and flagellum, which was missing from RFT. Higdon (1979) studied the effects of wavelength and amplitude changes of the flagellum (as did Dresdner, Katz & Berger 1980) and also the effects of changing spherical head dimension on both power and propulsive velocity. Phan-Thien, Tran-Cong & Ramia (1987) introduced the boundary-element method (BEM) for flagellar propulsion to account for non-spherical heads and non-slender flagella. These researchers derived optimal geometrical configurations for micro-organisms using helical flagellar motion, based on propulsive velocity and dissipated power. Cortez, Fauci & Medovikov (2005) introduced the regularized stokeslet method as a way of removing singularities from distributions of stokeslets and applied this to both BEM and infinitesimally thin flagella. An advantage of the regularized method is that it gives a bounded velocity field for simulations like ours where the head is modelled as a smooth surface and the flagellum by a simple line filament, or for simulations where the stokeslets distributed as a set of discrete, disconnected, points such as might be used to model a large number of suspended micro-organisms (Cisneros *et al.* 2007).

Many researchers have highlighted the significant effects of the presence of solid (or fluid) boundaries (Brenner 1962; Rothschild 1963; Blake 1971; Blake & Chwang 1974; Katz 1974; Fulford & Blake 1983; Gueron & Liron 1992; Ramia, Tullock & Phan-Thien 1993) on the motion of spheres, slender bodies, fixed cilia or swimming micro-organisms at low Reynolds number. One of the first studies to take into account the effect of solid boundaries on flagellar propulsion was Reynolds (1965) who used the early flagellum model of Taylor (1951) in the presence of a wall. Katz (1974) showed that an important feature of flagellar propulsion near a plane boundary was an increase in the ratio of normal to tangential resistance coefficients. Given that it is this ratio which determines flagellar propulsive force in RFT, and the values of the coefficients which determine power dissipation, this work suggested that the presence of walls must be included when considering cells observed between a microscope slide and coverslip. There are also many instances in the female reproductive tract where sperm are in close proximity to epithelial surfaces, or the ovum (Fauci & Dillon

2006). Ramia *et al.* (1993) undertook a thorough study of the effects of both a single wall, modelled by an image system, and parallel plates, modelled by an image system and discretized plate, on the locomotion of a swimming microorganism. Ramia *et al.* (1993) also undertook simulations of interactions between close swimming micro-organisms, as did Ishikawa *et al.* (2007), both using a BEM formulation. Recently, Cisneros *et al.* (2007) and Ainley *et al.* (2008) have applied the method of regularized stokeslets to flows bounded by a single wall, and Cisneros *et al.* (2007) to simulations of multiple interacting organisms.

Most previous studies of flagellar propulsion have, with the exception of Yundt *et al.* (1975) and Dresdner & Katz (1981), used prototype travelling waves to model the flagellar beat. Yundt *et al.* (1975) used high-speed cinematography to manually trace out actual flagellar beat and cell kinematics and compared these to predictions of cell kinematics using resistive-force theory. A significant technological advance since the work of Yundt *et al.* (1975) has been the advent of high frame rate digital video cameras that can be coupled with microscopy to obtain images of the flagellum throughout many flagellar beat cycles. In this paper, we use digital microscopy to measure approximate head morphology, kinematics and actual flagellar beat, on a number of sperm and compare the measured kinematics to those computed using a distribution of regularized stokeslets (Cortez *et al.* 2005) that discretize the sperm. The method of regularized stokeslets is appropriate as we model the sperm head as a discretized ellipsoidal surface and the flagellum as a slender filament. In addition, we follow Ramia *et al.* (1993) by noting that the effects of the microscope slide and coverslip walls are likely to be significant, given that the chambers used in clinical andrology are usually 20 μm deep, which is around half the length of the sperm. The results of Fulford & Blake (1983); Katz (1974); Ramia *et al.* (1993), amongst others, indicate the $C_t/C_{t\infty}$ and C_n/C_t ratios for rods translating parallel to and midway between slide chamber walls. Here, $C_{t\infty}$ is the tangential resistance coefficient in an infinite medium. For a 50 μm long slender rod, similar to the size of a human sperm flagellum (WHO 1999), these results indicate ratios of $C_t/C_{t\infty} \approx 1.18$ and $C_n/C_t \approx 1.78$ for a 50 μm deep chamber, and $C_t/C_{t\infty} \approx 1.39$ and $C_n/C_t \approx 2.09$ for a 20 μm deep chamber (values obtained by reading the BEM results in figure 4(*e*) of Ramia *et al.* 1993). We therefore also discretize the microscope slide chamber in our simulations.

The paper begins with a discussion of our hydrodynamic solution method for a flagellum and attached cell body, and verification of the computational method on translating sphere and rod test cases, as well as comparison with the propulsive velocity calculations of Dresdner *et al.* (1980) and Higdon (1979) and dissipated power calculations of Higdon (1979). We then introduce the walls of the microscope slide chamber into the simulation, and verify these calculations against the results summarized in Ramia *et al.* (1993). The paper proceeds with a calculation of propulsive velocity and trajectory, resulting from experimentally observed flagellar motions, and a comparison of these kinematics with experiment. In addition to using experimentally observed sperm for validation of the hydrodynamic code, we discuss predictions of sperm power dissipation. Finally, we use our method to predict changes to sperm kinematics and power consumption that result from hydrodynamic effects of changes to head geometry.

2. Hydrodynamic simulation method

Mammalian sperm, including those of humans, exhibit various swimming behaviours throughout their life, which are thought to be related to the different

stages of their journey through the female reproductive tract (Suarez & Pacey 2006). Briefly, following ejaculation, sperm motion is initially linear and progressive; whereas once sperm reach the uterine (fallopian) tubes, their pattern of movement changes to become more erratic and hyperactivated. While hyperactivated motility is thought to be important in the final stages of fertilization, this paper will examine the fluid mechanics of progressively motile sperm, since these are what are evaluated in semen analysis (WHO 1999) to determine the sperm that are capable of penetrating cervical mucus and therefore capable of entering the female reproductive tract (Aitken *et al.* 1985). The motile concentration of such sperm has been shown to be closely associated with predicting the probability of conception (Larsen *et al.* 2000).

The length of the human sperm flagellum L is around 50 μm (WHO 1999) and its radius a is 0.25 μm (Dresdner & Katz 1981); the head is approximately an ellipsoid of $5.8 \times 3.1 \times 1$ μm (Brennen & Winet 1977) – although human sperm display a large variability in head morphology. The straight line, propulsive velocity of sperm isolated from seminal plasma by density centrifugation and then observed in a simple salt solution is around 40–100 $\mu m\, s^{-1}$ (Mortimer 1994). The viscosity of semen is variable (Owen & Katz 2005), but for experiments in tissue culture, the fluid has a viscosity close to water at 37°C. The Reynolds number of the sperm cell during progressive motility is therefore of the order of 10^{-2} (Dresdner *et al.* 1980).

Given the very low Reynolds number, the inertialess Stokes equations are a useful approximation for the flow (Happel & Brenner 1981; Lighthill 1976). We define a local coordinate frame x–y, with x aligned along the head principal axis and the undeformed flagellum. The centre of this frame is the head centroid. We also define a fixed global frame X–Y. The unknown swimming velocity of the sperm is, in the local coordinate frame aligned with the head, $\boldsymbol{U}_p(t)$, and its angular velocity, $\boldsymbol{\Omega}(t)$. The head and flagellum are parameterized by position $\boldsymbol{r}(s,t)$, where s is a coordinate on the surface of the cell. The flagellum has 'beat' velocity $\hat{\boldsymbol{u}}(s,t)$, but the head does not beat. For planar motion of the cell (Brennen & Winet 1977), the velocity at any point on the cell is

$$\boldsymbol{u}(s,t) = \hat{\boldsymbol{u}}(s,t) + \boldsymbol{U}_p(t) + \boldsymbol{\Omega} \times \boldsymbol{r}(s,t). \tag{2.1}$$

The incompressible Stokes equations, pertinent to the flow, are

$$\mu \nabla^2 \boldsymbol{u} - \nabla p = \boldsymbol{f}, \quad \nabla \cdot \boldsymbol{u} = 0. \tag{2.2}$$

As the Stokes equations are inertialess, they do not admit accelerations. Consequently, the force $\boldsymbol{f}(s,t)$ and moment generated by the cell have to balance

$$\int_s \boldsymbol{f}\,\mathrm{d}s = 0, \quad \int_s \boldsymbol{r} \times \boldsymbol{f}\,\mathrm{d}s = 0, \tag{2.3}$$

where the integrals are over the entire surface of the cell (head, mid-piece and flagellum). This force balance is termed *zero-thrust* swimming (Lighthill 1976).

At each time point during a numerical simulation, this force balance is used to derive the unknown propulsive velocity that results from the flagellar motion. The Stokes equations are steady (Happel & Brenner 1981), but the propulsive velocity required for a force balance at any instant will vary with the instantaneous flagellar position and velocity. In this way the steady, inertialess Stokes equations can be used to calculate sperm acceleration. The zero force and moment balances are an integral part of the fluid solution procedure. This procedure generates a time-varying propulsive velocity, which can then be used to reconstruct the cell track, and a

time-varying force distribution, which may be used, via an application of the Stokes equations throughout the flow-field, to obtain the fluid flow-field velocities.

2.1. *Method of regularized stokeslets*

In order to solve the Stokes equations we use a very useful approximation of the regularized stokeslet due to Cortez (2001): the (unknown) velocity at any point s over the sperm cell surface is

$$u_j(s) = -\frac{1}{8\pi\mu}\sum_{n=1}^{N}\sum_{i=1}^{3} S_{ij}(s_n, s) f_{n,i} A_n, \tag{2.4}$$

where it is assumed that the cell has been discretized into N points, A_n is a corresponding quadrature weight (which may vary depending on whether the point is on the head, mid-piece or the flagellum), and $-f_{n,i}$ is the ith component of the force on the fluid applied at point n, which is an unknown. $S_{ij}(s_n, s)$ is the *regularized stokeslet* of Cortez (2001), which removes the singularity of the stokeslet.

$$S_{ij}(s_n, s) = \delta_{ij}\frac{r^2 + 2\epsilon^2}{(r^2+\epsilon^2)^{3/2}} + \frac{(x_i(s_n) - x_i(s))(x_j(s_n) - x_j(s_n))}{(r^2+\epsilon^2)^{3/2}} \tag{2.5}$$

with $r = ||\boldsymbol{x}(s_n) - \boldsymbol{x}(s)||$, and ϵ a small regularization parameter. The optimum value of ϵ is one which minimizes the velocity, or force, error for a particular discretization of the surface geometry (Ainley *et al.* 2008) and may be different between the head and flagellum (and walls if present). Choice of the regularization parameter is intimately involved with the choice of discretization and is discussed in § 2.2. In vector form, (2.4) is

$$\boldsymbol{u} = \boldsymbol{G}\boldsymbol{f}. \tag{2.6}$$

The problem is three-dimensional, with six unknowns (three translational and three rotational propulsive velocities) but only propulsive motion in the x–y plane is non-zero in our simulations: the tail motion is restricted to this x–y plane, and the problem is symmetrical about $z = 0$ as we simulate sperm swimming in either an infinite medium, or parallel to, and mid-way between parallel slide chamber walls. For each point on the cell, and on the slide chamber walls (if present), the velocity is split into a known beat velocity, zero-velocity boundary condition or component resulting from the unknown cell propulsive velocity. For planar motion, each cell point i has the x and y components of propulsive velocity (including angular velocity),

$$\boldsymbol{X}_i \boldsymbol{U}_p, \tag{2.7}$$

where

$$\boldsymbol{X}_i = \begin{bmatrix} 1 & 0 & -r_{yi} \\ 0 & 1 & r_{xi} \\ 0 & 0 & 0 \end{bmatrix} \tag{2.8}$$

and $\boldsymbol{U}_p = [U_{px}\ U_{py}\ \Omega]^T$. Concatenated into a vector comprising all the discrete points in the problem (i.e. on the cell head, flagellum and slide chamber walls), the velocity-boundary condition is $\boldsymbol{u} = \hat{\boldsymbol{u}} + \boldsymbol{X}\boldsymbol{U}_p$. Matrix $\boldsymbol{G}$ is inverted and we form the vectors

$$\boldsymbol{b} = \boldsymbol{G}^{-1}\hat{\boldsymbol{u}};\ \boldsymbol{a} = -\boldsymbol{G}^{-1}\boldsymbol{X}. \tag{2.9}$$

The x, y components of the vectors $\boldsymbol{b}$, $\boldsymbol{a}$ and the z component of $\boldsymbol{r} \times \boldsymbol{b}$, $\boldsymbol{r} \times \boldsymbol{a}$ are integrated over the surface of the cell to give $\boldsymbol{B}$, the components of force and moment resulting from the beat velocity, and $\boldsymbol{A}$, the components of force resulting from the

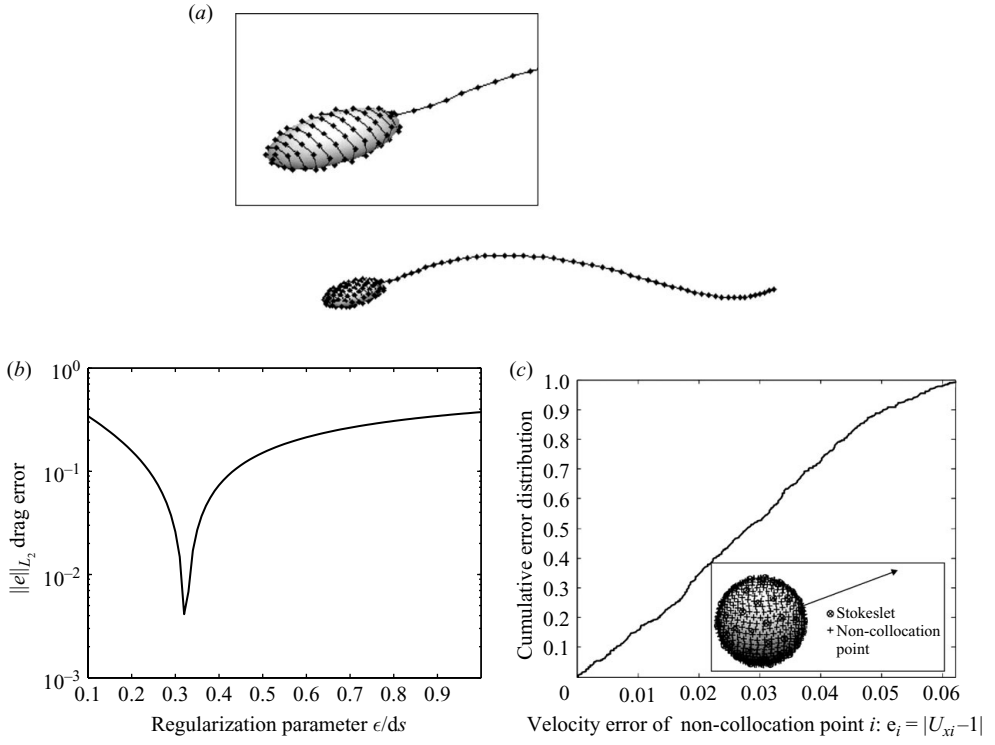

FIGURE 1. (*a*) Discretization of the head and flagellum (inset box shows the head in close-up). The dots are stokeslet positions. (*b*) L_2 regularization error for translating, head-shaped ellipsoids and 'flagella-like' rods. (*c*) Cumulative distribution of local velocity error for non-collocated points on the surface of a translating sphere. Collocated and non-collocated points are shown in the inset figure with an arrow showing the translation direction.

unknown propulsive velocity. As these forces and moments on the cell integrate to zero, finally, $\boldsymbol{U}_p$ is found from solution of

$$\boldsymbol{A}\boldsymbol{U}_p = \boldsymbol{B}. \tag{2.10}$$

2.2. *Spatial discretization, and regularization parameter for a free-swimming sperm*

Normal sperm are comprised of three distinct structural regions: the head, mid-piece and the flagellum. In our experiments, the mid-piece was difficult to distinguish from the proximal end of the flagellum, so, for the purposes of hydrodynamic simulation, we modelled the sperm with an ellipsoidal head and thin flagellum only. The method of regularized stokeslets may be applied to both infinitesimally thin flagella and spherical/ellipsoidal bodies, allowing us to investigate both the effects of tail beat and head morphology on the cell's fluid mechanics.

A human sperm head is, very approximately, a scalene ellipsoid (Brennen & Winet 1977), and it is computationally expedient to discretize the surface of the head by a strip, arranged in a spiral from the front of the head to the back (see figure 1*a*), much like an apple peel. In this way, a single coordinate s can be used to label points over the head (along the head 'peel') and along the flagellum. Alternative discretizations are also possible (Cortez *et al.* 2005), and we made sure that our simulations were not dependent on the discretization. The quadrature weights for the head are thus $ds \times p$, where p is the peel thickness. A standard head dimension of $5.8 \times 3.1 \times 1\,\mu\text{m}$

was used for validating our hydrodynamic simulation, but, in general, sperm may present a range of length/width ratios, some of which may be considered abnormal for clinical purposes by the relatively strict definition provided by WHO (1999). In our discretization, we keep the absolute size of ds and p the same, so that the area of each element on the head stays the same, regardless of head dimensions. The total number of patches on each modelled sperm head is therefore proportional to the head surface area. In this way we had a consistent method of discretizing heads of a range of dimensions (including a range of possible human sperm head morphologies and also spheres for comparison with the results of Ramia *et al.* 1993 and Higdon 1979). For our simulations, a step size d$s = 0.7\,\mu$m was chosen, and the thickness p was set at d$s/4$ so that the standard head dimension was discretized by 101 points. The discretization is such that each stokeslet force acts over approximately the same patch area on the head. Constant force discretization was used.

The natural way to discretize the flagellum, given that it is a thin, approximately inextensible filament is a series of equally spaced points along the flagellum. The force and moment balance for the flagellum, as an integral along a filament, has quadrature ds. The flagellum thickness of $0.5\,\mu$m only enters the computation in the choice of optimum regularization parameter ϵ, which is discussed below.

With this fixed discretization for all spheres, ellipsoidal heads and flagella that we wished to model, we were able to investigate an appropriate regularization parameter for the stokeslets on the cell. There is an optimum regularization parameter, which will give a minimum force, or velocity, error for a particular discretization (Ainley *et al.* 2008). Following the approach of Ainley *et al.* (2008) and Cortez *et al.* (2005), it is reasonable to choose a regularization parameter based on known exact results which are closely related to the problem at hand. To this end, we examined our predictions of drag on ellipsoids (of a range of dimensions similar to those of human sperm heads) and of thin rods (of a dimension similar to sperm flagella) translating in x and y directions in an infinite medium. We also studied the drag on spheres of a large range of sizes (larger than the range of sizes expected to be observed in a human ejaculate). The rods were modelled in the same way as the flagellum, and their exact solution was based on that of an elongated, needle-like ellipsoid (Happel & Brenner 1981). Figure 1(b) shows the L_2 error for all of the ellipsoid, sphere and rod drag simulations as the regularization parameter is varied. The L_2 error is defined as

$$||e||_{L_2} = \sqrt{\frac{1}{M}\frac{1}{D_{max}^2}\sum_{i=1}^{M} \mathrm{e}_i^2}$$

with the error $\mathrm{e}_i = D - D_o$, where D is the predicted drag force on the ellipsoid or rod, and D_o is the associated theoretical drag. While D_{max} is the maximum value of theoretical drag, M is the number of separate simulations used to optimize the error. We chose two isolated rod simulations (one longitudinal and one transverse translation) and two isolated ellipsoid simulations (both with an ellipsoid of dimension $5.8 \times 3.1 \times 1\,\mu$m, with one longitudinal and one transverse translation) to plot figure 1(b). The optimum $\epsilon = 0.32$ did not change when we varied the ellipsoid dimensions. This value is fixed for our particular discretization and is kept constant in all of our simulations.

Singular stokeslets alone may be used to model the flow around a cell body such as a sperm head by, for example, the highly accurate boundary-integral method. For the flagellum, a line distribution of singular stokeslets may not be sufficiently accurate

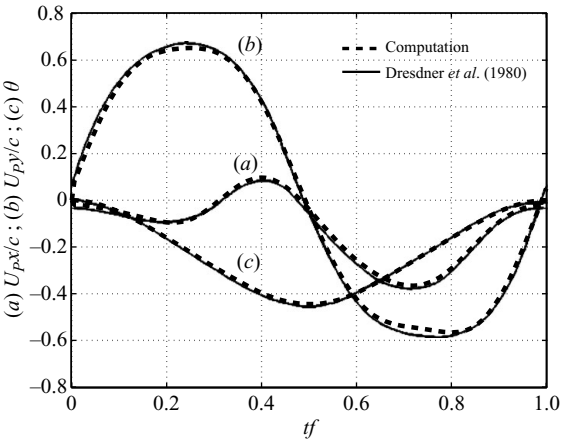

FIGURE 2. Computed temporal variation of (*a*) U_{PX}/c, (*b*) U_{PY}/c and (*c*) θ for a headless flagellum of shape given by $y = \alpha \sin k(x - ct)$ with $\alpha k = 1$, $n = 1$, over a beat cycle compared with the results of Dresdner *et al.* (1980).

to represent the flow around the slender-body and higher-order singularities may be required to give the desired accuracy in the near field. For example, see Dresdner *et al.* (1980) where the near field of the flagellum was modelled by stokeslets and stokes doublets but the far-field by stokeslets alone. The regularized stokeslet method, which we use here, causes each force to be spread over a small, smooth sphere rather than a single point (Cortez *et al.* 2005): this ensures that the near-field velocity error is small without recourse to higher-order singularities, such as Stokes doublets and dipoles. The cumulative local velocity error at non-collocated points, $e_i = |U_{xi} - 1|$ for a sphere, with $i = 1, \ldots, 500$, translating with velocity $U_x = 1$ is plotted in figure 1(*c*). Fifty per cent of these 500 non-collocated points have error less than 2.7 %, 90 % have error less than 5.0 %, and all have an error less than 6 %. Discretization and a choice of regularization parameter of the microscope slide chamber walls are discussed in § 2.4.

2.3. *Verification of the free-swimming sperm model*

The free-swimming model was verified by comparison with two test cases prior to comparison with the kinematics of experimentally observed sperm: the work of Dresdner *et al.* (1980) who plotted time histories of propulsive velocities for a free-swimming headless flagellum and the work of Higdon (1979) who undertook a thorough theoretical, hydrodynamic study of the effects of head size on flagellar propulsion and cell power consumption.

A comparison of the regularized stokeslet method with the results of Dresdner and Katz's headless flagellum is shown in figure 2. For this test case, the flagellum has fixed inextensible length L, radius a, and the y coordinate is $y(s) = \alpha \sin k(x(s) - ct)$, with $\alpha k = 1$ and $a/L = 0.01$. The wavelength of the flagellar motion is L. The travelling wave flagellum is discretized by $N = 50$ equally spaced regularized stokeslets along the flagellum. The velocity of the flagellum at these points was calculated analytically. In figure 2 we compare our results to those in figure 3 of Dresdner *et al.* (1980). The results show dimensionless propulsive velocity (in a global frame) and the orientation of the longitudinal axis of the flagellum. The comparison between our results and those of Dresdner *et al.* (1980) is shown to be generally very good.

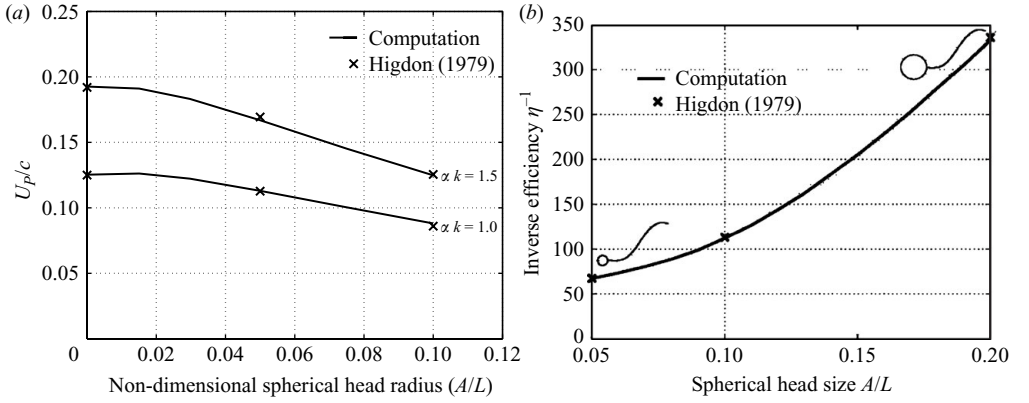

FIGURE 3. (*a*) Normalized average straight-line velocity U_p/c computed for a range of spherical head radius A/L values. Flagellar beat is a radially attached sinusoidal travelling wave. Crosses are results extracted from figure 5 of Higdon (1979), which compare well with our results (solid lines) using regularized stokeslets. (*b*) Predicted non-dimensional inverse efficiency η^{-1} for cells with a range of head size A/L and flagellar radius $0.01L$. Crosses are results extracted from figures 6 and 14 of Higdon (1979), which compare well with our results (solid lines) using regularized stokeslets.

To verify our prediction of the effect of head size on cell kinematics and power consumption we compare with the results of Higdon (1979). Higdon considered a distribution of stokeslet and dipole singularities along a helical, or planar, flagellar centreline, a stokeslet, dipole, and rotlet to model a spherical head, with an image system for the flagellum singularities at the spherical cell body centre. The flagellar wave studied by Higdon was a single-frequency travelling wave, attached radially to the spherical cell body. The range of spherical head sizes considered by Higdon ranged from $A/L = 0.05$ to $A/L = 0.2$. The smaller head sizes studied by Higdon approach the dimensions found in many species of spermatozoa – for example, human sperm, with dimension close to that of an ellipsoid of $5.8 \times 3.1 \times 1\,\mu\text{m}$ have a volume equivalent radius of $2.6\,\mu\text{m}$, which with a flagellar length of $50\,\mu\text{m}$ is $A/L = 0.052$. The longitudinal, translational, equivalent radius (Happel & Brenner 1981) for such an ellipsoid is $1.39\,\mu\text{m}$, giving $A/L = 0.028$. The same geometry was used as an input to our code, with the sperm head and flagellum discretized by regularized stokeslets, rather than by Higdon's exact method. This verification was necessary to show that our model could predict propulsive velocity as head morphology was varied.

Data read from Higdon's figure 5 were recast into a graph of spherical head radius A, non-dimensionalized by tail length L, versus straight line swimming speed U_p, non-dimensionalized by wave speed c, and shown in figure 3(*a*). The flagellum wave amplitude is α, and with fixed wavenumber $k = 2\pi/L$, the parameter αk is non-dimensional amplitude. Two different values of this amplitude parameter $\alpha k = 1,\ 1.5$, and a range of head sizes between headless and $0.10L$ were investigated. The two different computational methods reveal similar results, with Higdon's results represented as crosses, and our computations by solid lines in figure 3(*a*). We concluded that our model could adequately predict the hydrodynamic effects of changing head size.

Higdon (and Phan-Thien *et al.* 1987) also calculated dimensionless inverse efficiency

$$\eta^{-1} = \frac{\bar{P}}{(6\pi\mu\bar{A} + K_T L)\bar{U}^2}, \tag{2.11}$$

where $\bar{P}$ is the cycle averaged instantaneous power, $\bar{A}$ is the volume equivalent radius of the head, L is the flagellum length, $\bar{U}$ is the beat cycle average propulsive velocity and

$$K_T = \frac{2\pi\mu}{\log(2L/a)}. \tag{2.12}$$

Points from Higdon's figure 6 and figure 14 were combined to give the crosses on figure 3(*b*). The solid line is a prediction of cell power consumption using our regularized method with spatially discretized head. It is important that we verified our power calculations because power changes appreciably (Ramia *et al.* 1993) when cells are simulated in shallow chambers, like those used in our experiment (see § 3).

2.4. *Inclusion of microscope slide chamber walls*

For clinical purposes, human sperm are normally observed in chambers of 20 μm depth (WHO 1999) and, as such the cell swims between parallel walls that are often less than a flagellum length apart. We use the results of Ramia *et al.* (1993) to benchmark our computations of the effect of slide chamber walls. It was noted by Katz (1974) that forces on a flagellum increase in the presence of walls, and that the ratio of normal to tangential forces (the propulsive advantage) increases. However, head drag also increases close to walls, and this increase compensates for most of the propulsive advantage (Ramia *et al.* 1993). As a result, the presence of walls may not affect sperm kinematics significantly, assuming the flagellum beats in the same fashion, but will increase the power dissipation. To model the presence of walls, Ramia *et al.* (1993) used a system of images (a half-space) and a single, large discretized plate. Ainley *et al.* (2008) have recently derived an image system, including regularized doublets and dipoles, to enforce no slip velocity for a regularized stokeslet single wall case. Ainley *et al.* (2008) reported that there is no current regularized system for flow between two parallel plates, but this situation could be approximated by a regularized image system and a single discretized plate as in Ramia *et al.* (1993). Ramia *et al.* (1993) note that the same results can be achieved, albeit at the expense of the size of the computational problem, by two discretized plates. This is the simple approach we employ here: to discretize, using regularized stokeslets, a plate above and below the sperm, sphere or rod (the two cases we use to verify our method). As we use a regularized system of stokeslets, we only need to discretize infinitesimally thin plates.

To model the plates, we used a square regular grid of side length $2L$ with a grid step size $10 \times \mathrm{d}s$, meshed using Delaunay triangulation. To regularize the plate elements, we follow Ainley *et al.* (2008) who use a regularization $\epsilon = CA^m$, where A is the area of the surface element, and $m = 0.45$. $C = 0.28$ worked well in our test cases and was fixed for all further simulations. Ainley *et al.* (2008) note that there is no established convergence analysis for the regularized stokeslet method other than to compare the discretized, regularized system against known test cases: here, as in Ramia *et al.* (1993), we use the drag on a sphere translating between two plates and the drag on a rod translating in longitudinal and transverse directions between two plates. The test case rods were of the same size as the flagellum, and the test case spheres were of the same equivalent radius (Happel & Brenner 1981) as our standard sperm head. The values of sphere drag, and rod normal and tangential resistance coefficients were similar (within two per cent) for a larger plate or for finer discretization (as long as the regularization parameter for the plates was adjusted according to $\epsilon = 0.28A^{0.45}$ as above). The sphere drag predictions and rod tangential and normal resistance coefficient predictions were insensitive to rotation or movement of the sphere and rod test cases.

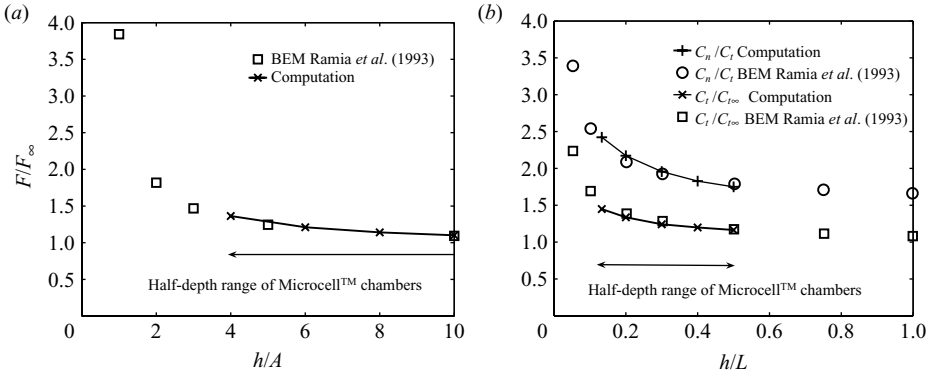

FIGURE 4. (*a*) Predicted increase in drag for spheres translating between parallel chamber walls. The chamber half-depth is h and A is sphere radius. Square markers indicate the results of Ramia *et al.* (1993), and the solid line with cross ($\times$) markers indicates our computations with spheres. (*b*) Predicted increase in $C_t/C_{t\infty}$ and C_n/C_t with varying chamber depth for a rod mid-way between chamber walls. The chamber half-depth is h and the rod length is L. Square markers indicate the $C_t/C_{t\infty}$ results; circle markers indicate the C_n/C_t results of Ramia *et al.* (1993); the solid line with cross markers indicates our computations of $C_t/C_{t\infty}$; and the solid lines with plus (+) markers indicate our computations of C_n/C_t.

Figure 4(*a*) shows the ratio of predicted drag for a sphere translating between plates to the exact drag ($6\pi\mu AU$) in an infinite medium. Our sphere simulation results are indicated by a solid line with cross markers. The results of Ramia *et al.* (1993) are shown as square markers in the figure. We only ran simulations which cover the range of depths of microscope slide chamber encountered in our experiments (the half-depth of these Microcell™ slides ranged from $h = 6\,\mu$m to $h = 25\,\mu$m in our experiments, which are detailed in the Appendix and discussed in § 3) and this range of depths is indicated in the figure. The comparison with the results of Ramia *et al.* (1993) is generally good over our range of interest.

Figure 4(*b*) shows our predictions of tangential and normal drag of a thin rod 50 μm long and 0.5 μm wide over the range of chamber half-depths h encountered in our experiments. The results are again compared to those of Ramia *et al.* (1993). We plot the ratio of tangential drag for the rod translating between plates to that of a rod translating in an infinite medium, $C_t/C_{t\infty}$. Following Ramia *et al.* (1993), we also plot the ratio of normal to tangential resistance C_n/C_t. Our $C_t/C_{t\infty}$ prediction is indicated by cross markers and a solid line and the corresponding results of Ramia *et al.* (1993) by square markers. Our predicted C_n/C_t ratio is represented by plus markers and a solid line, and the corresponding results of Ramia *et al.* (1993) by circle markers. The agreement is generally good with a slight underprediction of $C_t/C_{t\infty}$, and a consequent over-prediction of C_n/C_t ratio at shallow chamber depths. Overall, the same drag trends with increasing drag and a greater increase in flagellar propulsive advantage are shown with decreasing chamber depth.

3. Comparison of observed sperm kinematics with hydrodynamic prediction

To compare the results of our hydrodynamic code with the kinematics of sperm observed *in vitro* we took digital images of several sperm (three are described in this study) and measured both sperm head centroid position and flagellar position, which was used via numerical differentiation to estimate flagellar beat velocity. The

depth of field of the optics in our experiment was 4 μm, and sperm were observed as close to mid-way between the slide chamber walls as was possible to determine in our experiment. This mid-chamber focal plane was obtained by focusing on the slide chamber bottom and top (determined by the sharpness of focus of small scratches), and halving the number of turns of the microscope focus control. It was necessary to obtain clear images of the tail at a frame rate high enough that the tail position and beat velocity could be inferred along s. In our data, the distal end of the tail was sometimes difficult to identify clearly. However, in the majority of images, the tail was clearly focused and defined for its entire length, allowing us to define L and curve-fit a filament, length L, to the minority of images with out of focus or difficult to delineate tail images. In this way, we obtained tail position and beat velocity over a continuous time period. Head dimensions were traced out manually using the clearest images of the head. The head centroid position, and principal axis orientation were calculated automatically. The technical limitations of observing tail movement should not be underestimated: the system has to have images clear enough for accurate tail morphology, and hence an appropriate camera exposure has to be set. To numerically differentiate position, the camera has to operate at a high enough frame rate. The nominal beat frequency of human spermatozoa is around 10 Hz (Mortimer 1994) (although, in our experiments, we found this to vary significantly, and there were usually at least two to three higher harmonics present). A Nyquist limit of at least 60 Hz was judged to be the lowest possible frame rate, and this is possible using modern Computer-Aided Sperm Analysis (CASA) machines, but for the purposes of hydrodynamic analysis, this frame rate was doubled to at least 120 Hz to ensure that the beat velocity estimates were accurate enough (the actual camera frame rate was 121 Hz in our experiments). Details of the experimental method to obtain both sperm kinematics and the position and beat velocity of the flagella are discussed in the Appendix.

The beat velocity at point s, inferred from the time-varying flagellar position, is needed to determine the force the flagellum exerts on the fluid at that point. This beat velocity $\hat{\boldsymbol{u}}(s, t)$ may be determined via the numerical time derivative of the position of the flagellum $\boldsymbol{r}(s, t)$ of each imaged sperm. A 4-point centred difference of recorded position data was used to estimate the beat velocities. The raw data are at 121 Hz but smaller time steps of 0.005 s were used in the hydrodynamic solution method and so linear interpolation of the raw position and velocity was performed to obtain the flagellum position and beat velocity at any required time point. As the beat velocity is obtained via numerical differentiation of noisy position data, the predicted propulsive velocities obtained by the hydrodynamic analysis are also contaminated with noise. Yundt *et al.* (1975) suggest comparing computed tracks with experiment, rather than just comparing computed propulsive velocity, as the integrated velocity is less sensitive to noise.

Three individual, progressively motile sets of cell kinematics are discussed here. Cells σ_1 and σ_3 were chosen for display as they are both long tracks, and σ_2 was chosen because its track displays some 'looping' behaviour that we were intrigued to see if the fluid mechanics analysis also predicted. Cells σ_2 and σ_3 were studied in 12 μm chambers, and were therefore expected to show significant effects of chamber walls, and σ_1 in a 50 μm chamber. The effect of the chamber on σ_1 was therefore expected to be much less than for the shallower chambers. As well as simulations of spheres and rods, Ramia *et al.* (1993) undertook simulation of micro-organisms swimming next to walls and between parallel walls. Their results indicated that a flagellar propulsive advantage occurs when an organism swims close to walls, but that an increase in head

drag compensated for the propulsive advantage and so the cell propulsive velocities were not altered significantly. However, Ramia *et al.* (1993) pointed out that the power requirements for micro-organisms swimming between plates would be higher than for free swimming ones due to the increased forces on the head and flagellum. We ran the hydrodynamic simulation both with and without a model of the microscope slide chamber walls to investigate how the prediction of sperm kinematics and power consumption was affected. Although there were sperm–sperm interactions in the data set, σ_1, σ_2 and σ_3 were sufficiently far away from other cells (generally greater than a flagellum length) for no contact to take place. There should have also been little effect on these cells from the local velocity fields generated by other swimming sperm, as the velocity fields generated by a flagellum at this Reynolds number is only significant within a distance of the order of a flagellum length (Lighthill 1976). An exception was cell σ_2 which passed within half a flagellum length of an immotile cell. No motion of this extra cell was noted however, so the force on σ_2 was judged to be minimal.

The comparison is shown in terms of four sub-figures for sperm tracks σ_1 and σ_2. Sub-figure (*a*) shows the head orientation angle θ (which was integrated from the angular velocity), and sub-figures (*b*) and (*c*) show the propulsive velocities U_{px} and U_{py} in the local coordinate frame aligned with the head. Sub-figure (*d*) shows the integrated absolute velocity giving the sperm centroid track. It is to be expected that the head orientation angle and computed track will drift from the observed experimental data due to integrated errors. Following Yundt *et al.* (1975), we use a comparison of the predicted and experimental track as the most appropriate method for assessing the performance of the simulation. In addition to comparisons of instantaneous propulsive velocity and track, predicted power consumption for walled and unbounded simulations is plotted for each simulation. Only the track and power consumption comparison for the walled and unbounded simulations, are shown for cell σ_3. A viscosity of $\mu = 0.001$ Pa s was used in the simulations.

In figure 5, we show our simulation of sperm σ_1 with and without the presence of chamber walls and also the experimental kinematics for this cell. This cell was progressively motile and relatively fast. Its velocity along a 5-point running average track, based on a 30 Hz data sample and defined as the *VAP* (Mortimer 1994), was 105 μm s^{-1}, and the track length covered a period of 0.5 s. The head was approximated by an ellipsoid of standard, $5.8 \times 3.1 \times 1$ μm, dimension and the flagellar length was measured as 41 μm. The results for simulated head angle and lateral velocity are generally very good. There are significant higher harmonic components above the base beat cross frequency evident in both the experimental and simulated lateral velocity. The simulation of local longitudinal velocity is slightly less good, with a notable loss of accuracy at 0.3–0.35 s. In general, the local longitudinal velocity prediction is much more sensitive to noise in the measured flagellar beat. For both walled and unwalled simulations, the integrated track displays the same transition from 'triangular-like' waveform for the first two cycles of the track to a more 'square-wave-like' waveform. These same features are seen in the measured track and the shape of the track is quite well captured by the simulations. The dashed and solid lines are almost indistinguishable in figure 5(*a–c*), indicating that the simulation in the deep chamber and in an unbounded medium result in very similar kinematics. This similarity is to be expected since the chamber is relatively deep. The forces on the flagellum and head are, however, slightly higher for the walled simulation than for the simulation in an unbounded medium. These higher forces are evident in figure 6, which shows the predicted power consumption of this sperm. In this figure, dashed lines represent the results of simulation in an unbounded medium, and

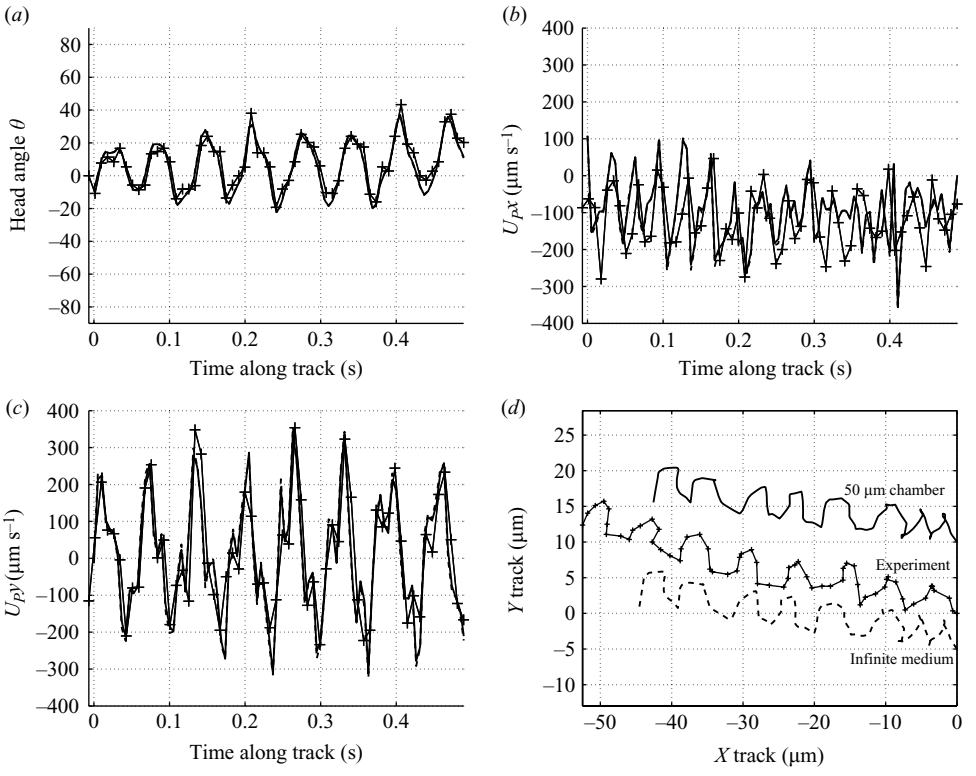

FIGURE 5. Comparison of computed and measured sperm kinematic parameters for sperm σ_1: (*a*) head angle θ (deg); (*b*) local (head-aligned) frame propulsive velocity U_{px}; (*c*) lateral velocity U_{py} (μm s^{-1}); (*d*) integrated track. The measured kinematic data are presented by thin lines with plus (+) markers, the computation including chamber walls is presented by thick solid lines and the computation ignoring chamber walls is represented by dashed lines.

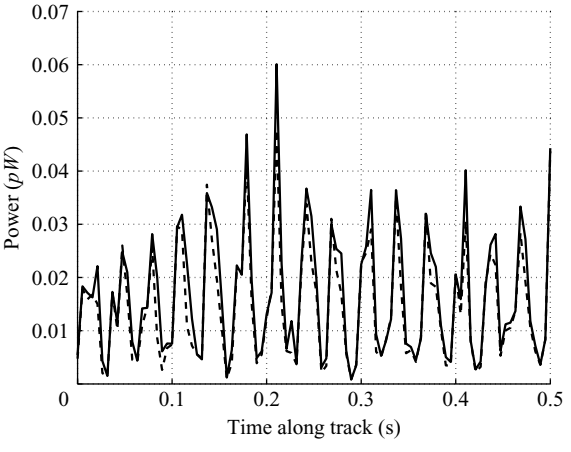

FIGURE 6. Comparison of the predicted power consumption of sperm σ_1. The solid line is the predicted power when chamber walls are included in the simulation; the dashed line is the result of a computation where the chamber walls are ignored. The mean power consumption in the walled case is 0.0168 pW, and the mean power consumption is 0.0145 pW when walls are ignored.

solid lines represent the results of simulation in a 50 μm deep chamber. Although the power differences between the two simulations are small, the sperm swimming in the chamber is predicted to consume more power than the sperm swimming in the unbounded medium. Our prediction of average power consumption for cell σ_1, which swam at a simulated 85 μm s^{-1}, is predicted to be 0.0168 pW in the chamber and 0.0145 pW in an unbounded medium. Cycle average power consumption was calculated by Dresdner & Katz (1981) using the formula

$$\bar{P} \approx (\mu f^2 L^3)\hat{p}, \tag{3.1}$$

where $0.4 < \hat{p} < 0.6$ is a dimensionless value dependent on the sperm morphology and flagellar beat, f is frequency and L is sperm length. Cell σ_1 has beat frequency 15.83 Hz and so Dresdner and Katz's formula gives a power prediction of 0.0102–0.0154 pW. Our unbounded simulation predicts a power consumption within this range. Phan-Thien *et al.* (1987) noted that the power consumption for a cell with a flagellum modelled by a travelling wave varies very little throughout the cycle; however, here the flagellum of σ_1 is close to undeformed, and almost stationary, at several time points (when it thus produces almost no propulsive velocity), and so its power consumption is oscillatory, unlike that obtained with a travelling wave.

During the data gathering experiments (see the Appendix), and in the hydrodynamic analysis, small-scale detail including loops and kinks in the track of some of the sperm were noticed. These small-scale details often coincided with low sperm velocity magnitude. A second sperm, σ_2, presented a track consisting of alternate sense loops of the head centroid at regularly spaced points. This cell was recorded in a shallow 12 μm chamber. We were intrigued to find out if the fluid mechanic simulation also demonstrated these loops. Sperm σ_2 was progressively motile, with $VAP = 41$ μm s^{-1}, flagellum length was measured at $L = 40$ μm and head dimensions were taken as $5.8 \times 3.1 \times 1$ μm. The data for this cell are shown in figure 7. Again, thin solid lines with plus markers denote the experimentally measured kinematics, dashed lines represent the simulation of this sperm swimming in an unbounded medium, and thick solid lines represent the simulation of the sperm swimming in the centre of a shallow 12 μm deep chamber. In this set of simulations it is evident in figure 7 that there is a slightly larger difference in the kinematics predicted with and without chamber walls – although the differences in the propulsive velocities (figure 7*a*) are still quite small. It can be seen in figure 7(*d*) that the integrated velocities produce a track length of 8.85 μm in the experiment, 6.50 μm when walls are included in the simulation, but only 5.68 μm when walls are ignored. The inclusion of chamber walls in the simulation increases the accuracy of the track in this case. It is evident that the fluid simulation also demonstrates loops (of the same sense and approximate size) as are present in the experimental data. The fluid mechanical modelling demonstrates that these loops in the track are a feature of this sperm's, approximately planar, flagellar beat, and are not caused by out-of-plane rotation of the head. While sufficient for satisfying the Nyquist sampling criterion, the sampling rate in the experiments was still relatively low and there are only about six data points per wavelength in figure 7(*a–c*). This sampling is adequate for assessment of the wavelength, where the agreement between simulated and experimental track is excellent, but there is an inevitable data loss that will affect amplitude more significantly. The simulation reproduces the important features of the experimental track with good overall fidelity. Head angle prediction θ (figure 7*a*) is similar for both simulations and shows slight, brief deviations from experiment (up to 7°) early and very late in the track. Simulated lateral velocity U_{py} in figure 7(*c*) is slightly higher when the walls are ignored but the

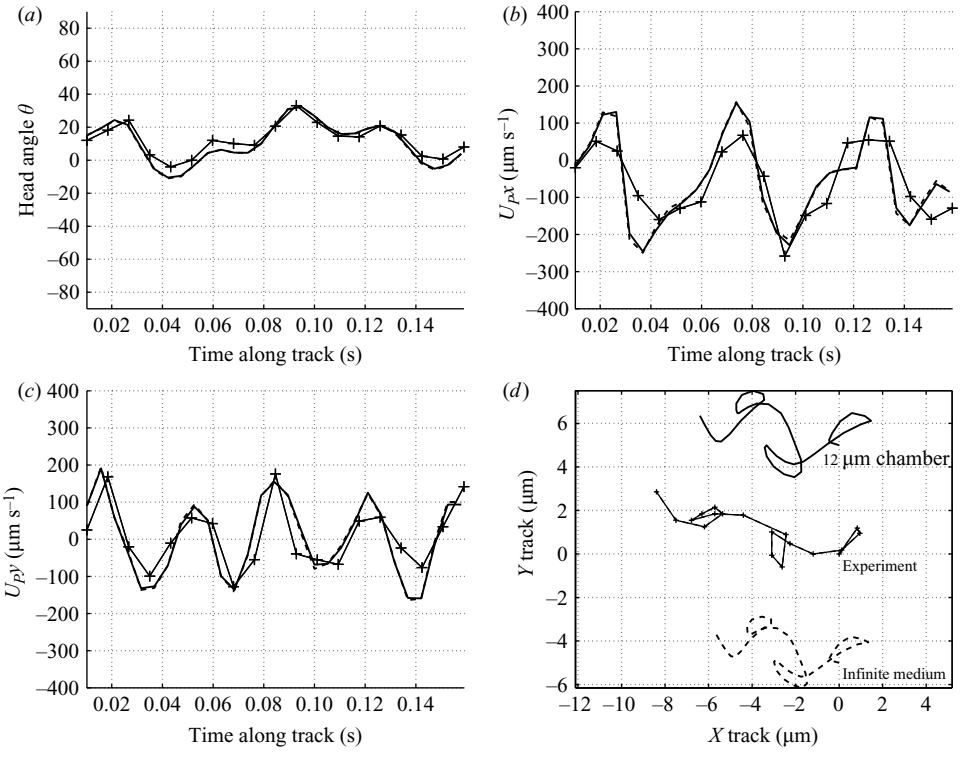

FIGURE 7. Comparison of computed and measured sperm kinematic parameters for the 'looping', progressively motile, sperm cell σ_2: (*a*) head angle θ (deg); (*b*) local (head-aligned) frame propulsive velocity U_{px}; (*c*) lateral velocity U_{py} (μm s^{-1}); (*d*) integrated track. The measured kinematic data are presented by thin lines with plus (+) markers; the computation with chamber walls is presented by thick solid lines; the computation in an unbounded medium is presented by thick dashed lines. Note the similarity between the computed and measured track topologies in (*d*), especially with regard to the looping behaviour. The tracks move, broadly, from right to left.

peak-to-peak velocity amplitudes of the simulation and experimental data are similar throughout; predicted x velocity, U_{px} in figure 7(*b*), is more retrograde than is seen in the experiment, and the peak-to-peak velocity amplitude of the experimental data is smaller on average. Furthermore, the U_{px} traces suggest the existence of a higher-frequency component which would be affected more significantly by the low sampling rate and this may partly explain the inferior amplitude prediction than for U_{py}. The predicted track topologies in figure 7(*d*) show all the features of the experimental data including the loops referred to earlier. With this very shallow chamber, however, there are large differences in the predicted power consumption (shown in figure 8) between the walled and unbounded simulations. In the walled simulation, the power consumption is 0.0127 pW, which is likely to be close to the actual power consumption of the sperm, but it is underestimated by almost fifty per cent, with an average of 0.0084 pW, when walls are ignored. Again, it can be seen that the instantaneous power consumption varies throughout the beat cycle. Cell σ_2 has beat frequency component of 11.22 Hz contributing 70 % of the tail amplitude and a component at 15.24 Hz contributing 30 % of the amplitude and so (3.1) gives a power prediction of 0.006–0.009 pW.

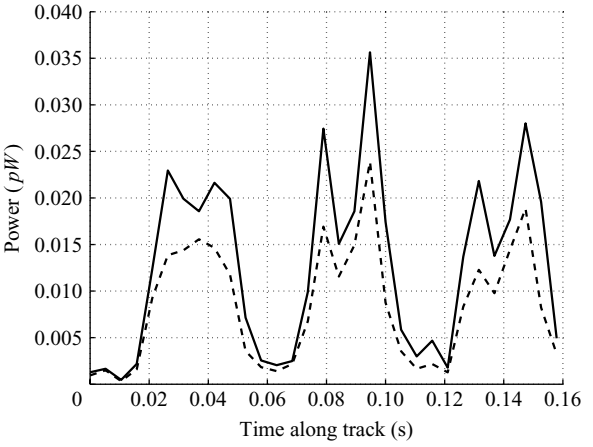

FIGURE 8. Comparison of the predicted power consumption of sperm σ_2. The solid line is the predicted power when chamber walls are included in the simulation; the dashed line is the result of a computation where the chamber walls are ignored. The mean power consumption in the walled case is 0.0127 pW, and the mean power consumption is 0.0084 pW when walls are ignored.

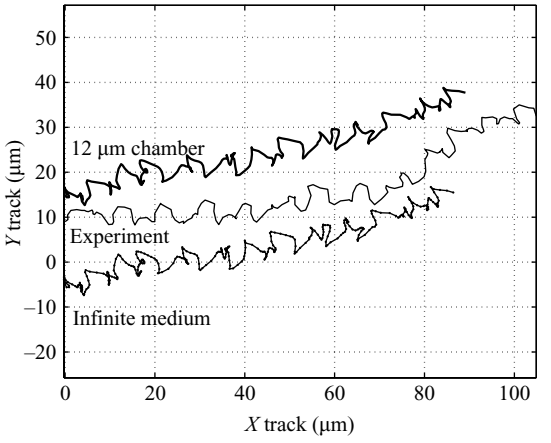

FIGURE 9. Comparison of the predicted tracks of sperm σ_3. The solid line is the predicted track when chamber walls are included in the simulation; the bottom line is the result of a computation where the chamber walls are ignored. The thin solid line is the experimentally recorded track.

To further investigate the increased power consumption in shallow chambers and to compare our simulation to a long track, we also present data for a third sperm, σ_3, in figure 9. This sperm was progressively motile (with an average path velocity $VAP = 76\,\mu\mathrm{m\,s^{-1}}$) over approximately two seconds. The length of the flagellum for this case was measured at 46 μm and the head was approximated by the standard dimensions of $5.8 \times 3.1 \times 1$ μm. Sperm motion is broadly from left to right in the figure. Three tracks are shown: the thin solid line is the experimentally recorded track; the thick solid line is the computation where the effects of the chamber walls are included; the thin solid line with dots is the result of a computation where wall effects are ignored. The features of most of the cycles are well captured by the simulations, with some distinctive small-scale features common to both the experiment and the

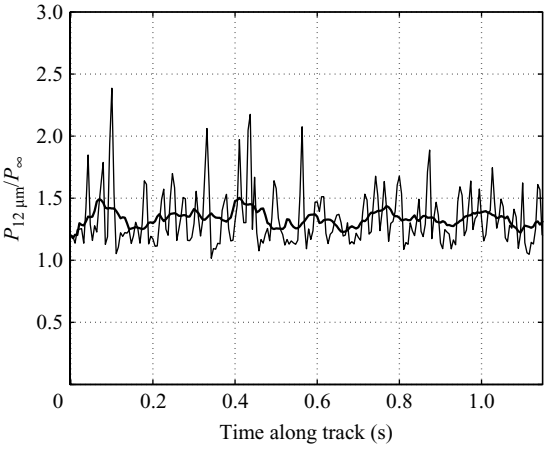

FIGURE 10. Ratio of the predicted power consumption of sperm σ_3 with walls included to that with walls ignored. The thick solid line is a 'cycle-' averaged ratio, and the thin solid line is the instantaneous power ratio. The average increase in power consumption is 32 %.

simulations. It must be remembered that the hydrodynamic code only has the planar x–y tail beat motion and position as an input, and does not record out-of-plane head rotation (which we could not measure accurately). The hydrodynamic analysis therefore shows that these small-scale track details are largely the result of complexity in the (planar) tail motion, and not solely due to out-of-plane head rotations. The experimental track is 107 μm long, the simulation including chamber walls produces a track 93 μm long and the simulation where walls are ignored produces a track 89 μm long. The mean power consumption is 0.0090 pW when chamber walls are included, and when walls are ignored it is 0.0068 pW. The presence of walls only 6 μm above and below the cell increases the power by 32 %. The ratio of instantaneous power consumption between the walled and unbounded simulations is shown in figure 10. Cell σ_3 has beat frequency component of 6.6 Hz contributing 50 % of the tail amplitude and a component at 11.84 Hz contributing 50 % of the amplitude and so (3.1) gives a power prediction of 0.0051–0.0076 pW. All of the predicted tracks were shorter than the experimentally recorded tracks, indicating that the computed average propulsive velocities are slightly lower than in the experiment.

4. Analysis of a prototype sperm

Cell σ_1, which had the least evidence of the effect of chamber walls, produced the most regular track and so a section of tail data for this cell was extracted and fourth-order polynomials in s fit, in a least squares sense, to produce a prototype cycle of noise-free flagellum motion. This prototype flagellum was used to investigate the flow-field resulting from flagellar propulsion and the effects of changes to head dimension on sperm kinematic parameters (assuming constant flagellar motion).

4.1. *Flow-field of a swimming sperm*

Lighthill (1976) argued that flagellar hydrodynamics analysis should go beyond the velocity of the organism to flow-field analysis as well. This argument is especially true if interactions between cells are of interest, as is often the case in a semen sample. Although no interactions were present in our data, we show velocity vectors for the prototype of σ_1, simulated in an infinite medium, to indicate the extent of disturbances

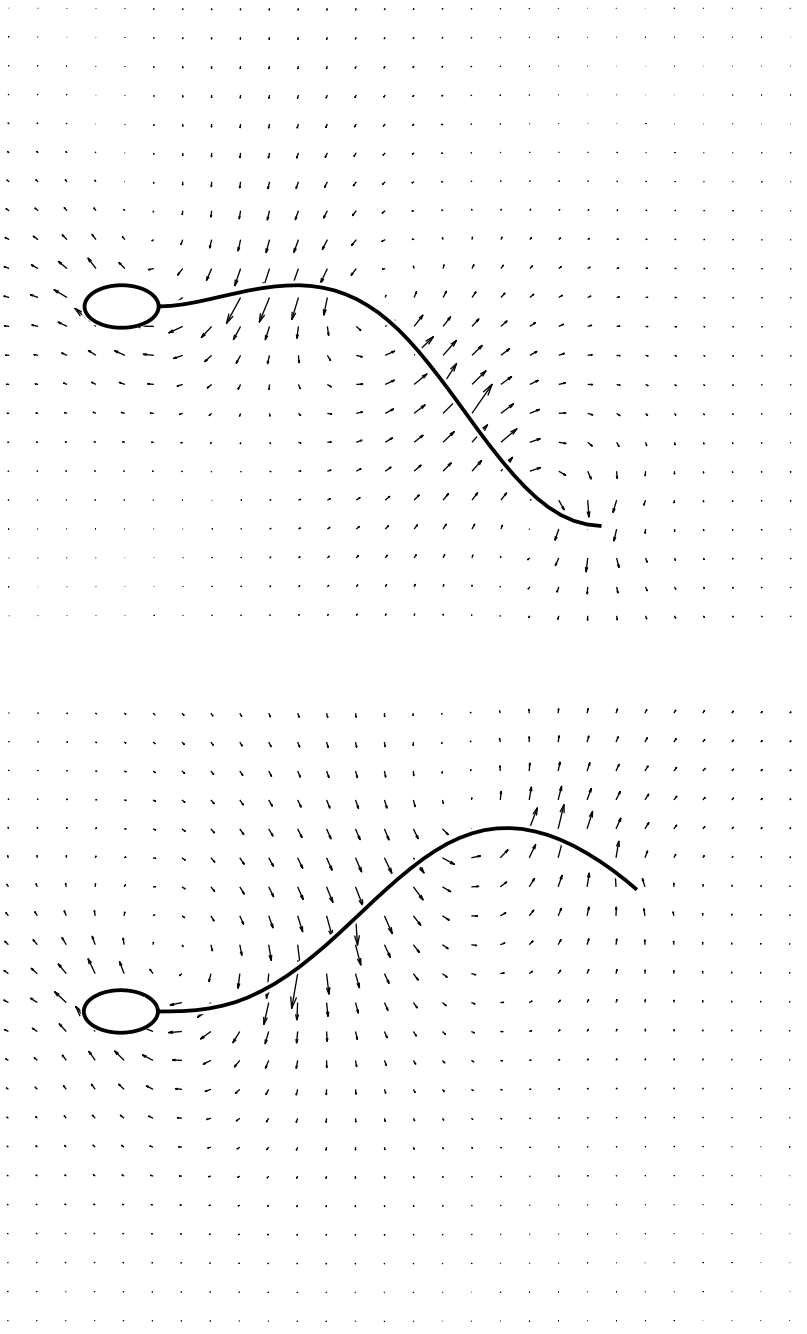

FIGURE 11. Velocity vectors for the prototype σ_1 at two time points 0.02 s, or 30 % of a flagellar beat cycle apart. The local vortices shown move down the flagellum as the beat progresses.

to the flow-field generated by the sperm in figure 11. The figure is plotted in a fixed global reference frame such that the velocity vectors at the head are equal to the propulsive velocity. The flow is highly localized about the flagellum as is predicted by Lighthill, and also seen in the results of (Higdon 1979), consisting of counter rotating

vortex structures (see Gray's figure of the local flow about a swimming nematode pictured in Lighthill 1976), which move down the flagellum as the beat progresses. Lighthill (1976) pointed out that these zero-thrust flow-fields have a local character, extending a distance considerably less than a wavelength from the flagellum. Although the velocity from a single stokeslet decays with $1/R$, Lighthill (1976) showed that a distribution of stokeslets with strength varying sinusoidally with x, as is the case with a travelling wave flagellum, decay almost exponentially with distance R from the x axis. This local character, and indeed the counter-rotating vortex structure, is clearly evident in the computed flow-field. The flow-fields (like those of Higdon 1979; Dresdner & Katz 1981; Fauci & Dillon 2006) show the dominance of normal over tangential forces: lengths of the flagellum that are moving in the normal direction are associated with large flow-field velocity (and force); lengths of the flagellum moving tangentially are associated with low velocity.

4.2. *Effects of head morphology on sperm hydrodynamics*

Human sperm are pleomorphic and so have a wide range of head sizes and shapes, both within and between individuals, compared to most other species . A relatively low level of sperm competition in humans is thought to allow such pleomorphy to persist (Birkhead 2000). Head aspect ratio and size is assessed for clinical purposes by analysis of stained images of fixed (dead) sperm and a fertility assessment of the sample includes a count of the proportion of sperm that have heads within the size and length/width definitions proposed by WHO (1999). It is certainly the case that a population of sperm with 'normal' flagella will have a distribution of head sizes and morphology. Length/width ratio affects the translational and rotational mobility of a body in Stokes flow (Kim & Karilla 1991), and so sperm heads of different dimensions will experience different resistances. The effects of changing head dimensions may be investigated using our prototype model of flagellar motion. This study was motivated by an empirical evidence that suggests that the effect of head shape on sperm hydrodynamics is considerable (Gomendio *et al.* 2007).

The hydrodynamic effects of head aspect ratio are complicated (Higdon 1979; Phan-Thien *et al.* 1987), but may be summarized by their effects on two important kinematic parameters: the straight-line velocity VSL, which is defined as the distance between the start and finish of the track, divided by the time taken to swim the track; and the amplitude of lateral head movement ALH (Mortimer 1994), which is defined as the lateral deviation of the track (peak to peak) about its average path (i.e. double the amplitude). These simulations are presented for an infinite medium: the trends in the results are the same when the cell swims between plates. An exception is the calculation of cycle average power consumption, which does change appreciably when simulations are run with and without walls.

It is interesting to note that via a statistical analysis of red deer (*Cervus elaphus hispanicus*) sperm head length/width ratio and VSL, Gomendio *et al.* (2007) found that sperm with head dimensions of high length/width ratio swim faster than those with lower length/width ratio. We wanted to investigate this experimental observation of Gomendio *et al.* (2007) using a hydrodynamic simulation rather than looking at the statistics of a population of sperm. As a summary of these computations of the effect of head length/width ratio on VSL, we present figure 12(a), which is a comparison of the VSL for several different heads attached to the prototype flagellum of sperm σ_1. The VSL is kept dimensional in the figure as that is the form most usual in semen analysis. We note, however, that head length/width ratio can be varied in a number of ways: e.g. by keeping the head length constant and

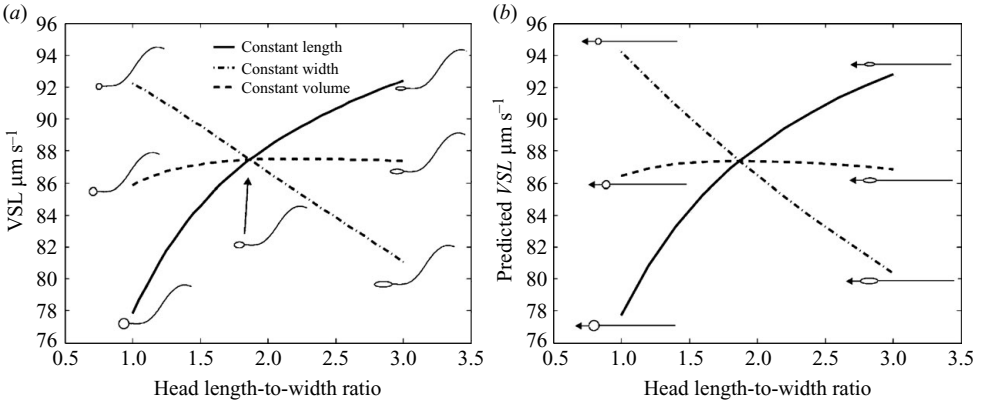

FIGURE 12. (*a*) Straight-line velocity *VSL* for variations in head length/width for the prototype flagellum σ_1. Simulations are presented for constant head length 5.8 μm (the solid line), for constant head volume $= \frac{4}{3}\pi 5.8 \times 3.1 \times 1$ μm^3 (the dashed line) and for constant head width 3.1 μm (the dashed-dotted line). Caricatures next to the curves show comparative sperm head sizes. (*b*) Predicted *VSL* using an axial resistance model of ellispoidal head and constant force generating rod-like flagellum $U = F/(6\pi\mu R + K_T L)$. Here, R is the equivalent radius of ellipsoids of constant x axis length 5.8 μm (the solid line), constant volume $= \frac{4}{3}\pi 5.8 \times 3.1 \times 1$ μm^3 (the dashed line) and constant y axis width 3.1 μm (the dashed-dotted line). Caricatures next to the curves show comparative ellipsoid and rod sizes and direction of translation.

varying head width; by keeping the volume of the head constant but varying the length/width ratio and by keeping the head width constant and varying the head length. Each method of changing the head length/width ratio has a different effect on the *VSL* of the simulated sperm. Caricatures are drawn in figure 12(*a*) to indicate the approximate dimensions of the simulated sperm. The computations at constant head length (the solid line in figure 12*a*) were run with a fixed head length of 5.8 μm; the computations at constant head width (the dashed-dotted line in figure 12*a*) were run with a fixed head width of 3.1 μm and computations at constant volume (the dashed line in figure 12*a*) were run such that the volume of the head was equivalent to that of an ellipsoid of $5.8 \times 3.1 \times 1$ μm^3. All of the lines therefore intersect at a nominal head dimension of $5.8 \times 3.1 \times 1$ μm. The head depth of 1 μm was kept constant in all simulations.

Our modelling is consistent with the observation of Gomendio *et al.* (2007) that sperm with high head length/width ratio swim faster. We show that, for the solid line in figure 12(*a*), narrower sperm (high head length/width ratio) have higher *VSL* than thicker sperm (low head length/width ratio) for constant head length. That is, narrowing the head is seen to increase the sperm *VSL* if the associated head length is kept constant. We suggest that this is the effect seen, statistically, by Gomendio *et al.* (2007). Gomendio *et al.* (2007) postulated that 'elongated' heads have less resistance to forward motion. However, at this low Reynolds number, it is shown by the dashed line in figure 12(*a*) that true elongation of the sperm head by stretching its length and narrowing its width (to retain constant volume) has very little effect on the fluid resistance of the head. Here there are two competing effects on the axial resistance (Kim & Karilla 1991): the axial resistance increases with head length, but drops with a decrease in head width. The two effects broadly cancel. There is, however, a slight increase in *VSL* for this type of head elongation, but there is no appreciable 'streamlining' effect at this low Reynolds number. Indeed, for simulations where the

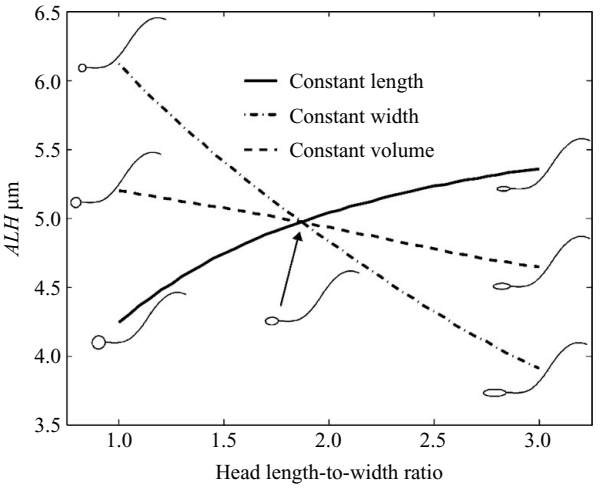

FIGURE 13. Amplitude of sperm lateral head movement ALH for variations in head length/width for the prototype flagellum σ_1. Simulations are presented for constant head length 5.8 μm (the solid line), for constant head volume $= \frac{4}{3}\pi 5.8 \times 3.1 \times 1$ μm^3 (the dashed line) and for constant head width 3.1 μm (the dashed-dotted line). Caricatures next to the curves show comparative sperm head sizes.

head is elongated, while keeping head width constant the dashed-dotted line of figure 12(a) shows that VSL is reduced.

Sperm with heads of different aspect ratio and size have different axial, transverse and rotational resistances. The dominant effect on VSL of changes to the axial resistance is illustrated by considering a simplified 'axial resistance' model where the sperm is modelled as an ellipsoidal head and straight, non-beating flagellum assumed to provide a constant axial propulsive force. For this simplified model, this propulsive force must equal the drag on an ellipsoidal head and straight flagellum, which is assumed to be (Phan-Thien *et al.* 1987)

$$F = (6\pi\mu R + K_T L)U, \tag{4.1}$$

where R is the equivalent radius (Happel & Brenner 1981) of the ellipsoid and $K_T = 2\pi\mu/\log(2L/a)$. For our sperm, the standard head size has $R = 1.39$ μm and $L = 45$ μm and $a = 0.25$ μm. In our simulations, the standard size sperm has a straight-line velocity of 87.49 μm s^{-1}, and so, for our simple model (4.1), we assume that the flagellum generates a constant force $F = 6.495 \times 10^{-12}$N which will be able to propel the ellipsoid and rod along at this same speed. We then use the axial resistance model (4.1) to predict straight-line propulsive velocity U as head dimension, parameterized by the equivalent radius R, is varied. The results of this simple model are shown alongside the VSL predictions of the hydrodynamic simulation in figure 12(b). A comparison of figure 12(a) and (b) shows that this simple axial resistance model gives a reasonable prediction of trends in straight-line propulsive velocity.

There are, however, slight differences in the curves for figure 12(a) and (b) as we would expect, given that the sperm yaws and translates laterally also. Figures 13 and 14 show the effects of varying head dimension on the sperm amplitude of lateral head movement ALH and maximum yaw angle $|\theta|_{max}$ during a flagellar beat cycle. These figures are plotted with the same format as figure 12. Kim & Karilla (1991) note that transverse resistance also scales with length, and it is this change in resistance

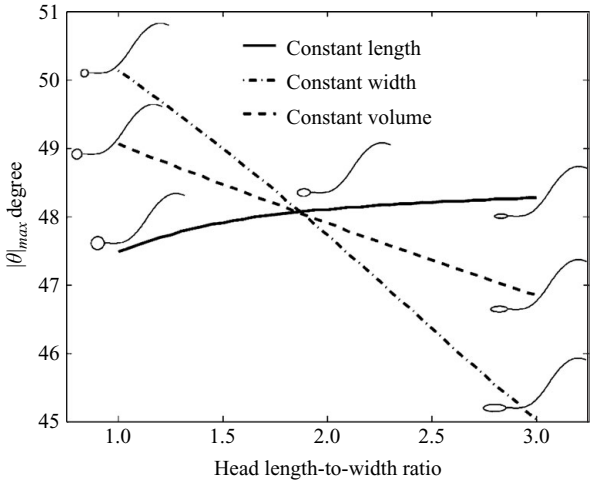

FIGURE 14. Maximum sperm head yaw angle $|\theta|_{max}$ for variations in head length/width for the prototype flagellum σ_1. Simulations are presented for constant head length 5.8 μm (the solid line), for constant head volume $= \frac{4}{3}\pi 5.8 \times 3.1 \times 1$ μm^3 (the dashed line) and for constant head width 3.1 μm (the dashed-dotted line). Caricatures next to the curves show comparative sperm head sizes.

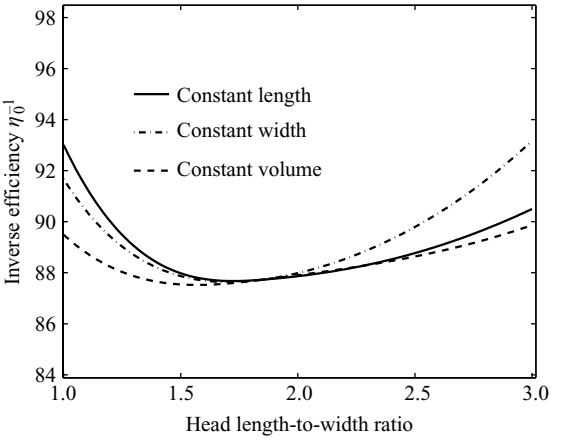

FIGURE 15. Predicted inverse efficiency η_0^{-1} of sperm in an infinite medium as head dimensions are varied. Simulations are presented for constant head length 5.8 μm (the solid line), for constant head volume $= \frac{4}{3}\pi 5.8 \times 3.1 \times 1$ μm^3 (the dashed line) and for constant head width 3.1 μm (the dashed-dotted line).

which explains the reduction in lateral movement with increasing head length. The discussion in Kim & Karilla (1991) is also instructive when considering the effects of head dimension on sperm yawing. They note that rotational resistance is sensitive to length and scales as L^3. An increase in head length produces a decrease in yaw angle as is seen in figure 14. The head length in our simulation changes by a factor of 3; however, the total sperm length changes by only around 12 %. The rotational resistance of the head and flagellum will scale as $(L + l_h)^3$, which for small (l_h/L) is approximately linear in l_h/L.

Figure 15 shows the power consumption of the sperm as their head dimensions are varied. The inverse efficiency is calculated, as in Higdon (1979) and Phan-Thien *et al.*

(1987), as

$$\eta_0^{-1} = \frac{\bar{P}}{6\pi\mu\bar{A}\bar{U}^2}, \tag{4.2}$$

where $\bar{A}$ is the volume average radius of the head (Phan-Thien *et al.* 1987). Although the inverse efficiency curve is quite flat, there are minima in the curves close to the 'standard' sperm head aspect ratio. The observation that the power curves are 'U-shaped' means that there is a sperm head aspect ratio for maximum efficiency. In an infinite medium, we predict this maximum efficiency to occur at a head aspect ratio of around 1.57 for the constant volume line, 1.7 for the constant width line and 1.72 for the constant length line of figure 15. These maximum hydrodynamic efficiencies occur at a head dimension range very close to 1.50–1.75 regarded as normal morphology by WHO (1999).

5. Conclusions

Digital microscopy was used in this paper to obtain the flagellar beat velocity and head centroid position of several human spermatozoa. The observed kinematics of these cells were compared with the predictions of a hydrodynamic method based on the method of regularized stokeslets. In order to implement the hydrodynamic method, an ellipsoidal head and flagellum were discretized, and chamber walls were also discretized in some simulations. These walled simulations were for a cell swimming exactly half-way between parallel walls. Power consumption was estimated and was found to be higher for simulations where walls were included. However, the kinematic parameters were not largely affected by the presence of walls.

The kinematics and resulting tracks of the sperm, measured at high frame rate, are complicated and individual cells can move between square-wave-like and triangular-wave-like or other shaped tracks. These details are reproduced by the hydrodynamic model despite the fact that only two dimensions (planar) tail motions were observed. Fine detail in the tracks is also captured in some cases. Transverse velocity and yaw angle were very well captured in all simulations, but average forward propulsive velocity was underpredicted compared to experiment. Given that the model does not underpredict forward propulsive velocity when applied to travelling wave test cases (which do not require numerical differentiation of tail position to infer beat velocity), it is postulated that the underprediction of forward progressive velocity of the experimental cases indicates sensitivity to noise, or missing information, in the tail data. For example, some of the propulsive velocity measured in experiment could have been due to intrinsic three-dimensional tail motion of the sperm. Any out-of-plane motions could not be measured in our experiment.

Power consumption calculated for the sperm was very much dependent on whether slide chamber walls were included in the simulation – for the shallowest chambers we tested, our power prediction was up to 50 % greater when walls were included. We can conclude that calculations of power expenditure for sperm in Microcell^{TM} chambers, or between slide and coverslip, should take chamber walls into account. It is important to understand better the effect of finite chamber depth since current international guidelines for human sperm observation suggest that only chambers of depth 20 μm and above may be used during laboratory analysis for clinical purposes. However, we note a moderate increase in power consumption of our simulated sperm even at this chamber depth.

Human sperm are pleomorphic, so even sperm with healthy, normal flagella display a range of head size and shape. For clinical purposes, head dimensions, which are important parameters in defining sperm function (WHO 1999), are obtained from stained images of fixed (dead) sperm. A prototype model of one of the sperm was used to investigate the effects of head shape on the propulsive velocities for complete cycles of flagellar motion. The present fluid mechanical analysis suggests that head dimension is a factor in determining the progressive velocity and amplitude of lateral head movement and yawing of the sperm (all other aspects of the flagellar motion being equal). Narrow heads have the highest forward progressive velocity. Heads with short lengths have a large lateral movement compared to longer heads. Elongation of the sperm head, while keeping the head volume constant, only has a small beneficial effect on *VSL*. However, minima in the power consumptions for these simulations were found where the sperm have 'normal' aspect ratio (an aspect ratio between 1.5 and 1.75). This suggests that the range of aspect ratios assessed as being 'normal' also correlates closely with the most efficient hydrodynamic range of aspect ratio. This paper addresses the fluid mechanical effect of these head variations for a fixed flagellar motion, and should therefore be of some use to andrologists by informing them of the fluid mechanical effects of head dimension on sperm kinematics. In actual sperm populations, however, some head abnormality and variations in head size may be accompanied by abnormal flagella size or function. This paper does not address changes to the flagellar beat that may be associated with abnormalities of the head. We have only studied forward progressive motion here, and it may be that the head has beneficial hydrodynamic effects for hyperactivated motility.

This work was funded by the Medical Research Council under the Discipline Hopping Scheme (grant G0001205) and Scottish Enterprise under the Proof of Concept Scheme (project reference 4-BPD007). Richard Cannon was also supported by the Royal Society of Edinburgh and Scottish Enterprise under the Enterprise Research Fellowship initiative. Assistance with the preparation of semen samples was provided by Matthew Fletcher and Daniel Smith of the Andrology Laboratory, Sheffield Teaching Hospitals. The authors are grateful to Professor Tim Birkhead (Department of Animal and Plant Sciences, University of Sheffield) for critical comments on the draft manuscripts.

Appendix: Details of the data-capture experiment

Human spermatozoa were obtained from patients and donors attending the Andrology Laboratory located in the Jessop Wing of the Royal Hallamshire Hospital, Sheffield, UK. Procedures were approved by the South Sheffield Research Ethics Committee (protocol number 04/Q2305/30) and informed consent to make digital video recordings of spermatozoa was obtained from each male donating a specimen to this study. For each specimen provided, the sample was collected by masturbation into a sterile, wide-mouthed container (Sarstedt Ltd, Leicester, UK) following a period of 3–5 days sexual abstinence. Following production, each sample was kept at a temperature of 37 °C for 30 min before routine procedures of semen analysis were performed according to World Health Organization (WHO) guidelines (WHO 1999). If the specimen was found to be normozoospermic at semen analysis, a highly motile suspension of spermatozoa was obtained from the remainder of the sample by density centrifugation of a 1 ml aliquot of liquefied semen through a Percoll gradient as described by Mortimer (1994). The final concentration of spermatozoa obtained was

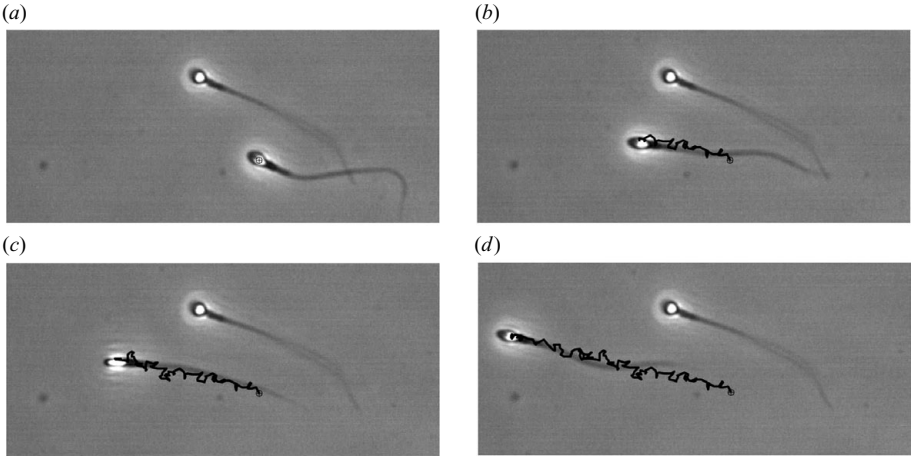

FIGURE 16. Sequence of still digital video camera images showing a swimming sperm and measured track (the solid black line): (*a*) start of the track; (*b*) position and track after 0.48 s; (*c*) position and track after 0.96 s; (*d*) position and track after 1.44 s. The other sperm in the image is immotile.

adjusted to approximately 20 million sperm per ml in Earle's Balanced Salt Solution (EBSS) (Sigma Chemical Co., Poole, UK) containing 0.3 % (w/v) human serum albumin (Sigma Chemical Co., Poole, UK). Sperm preparations were maintained in a humid atmosphere at 37 °C in 5 % CO_2 for up to six hours prior to being observed. Samples were placed into Microcell™ slides (Conception Technologies, San Diego, USA) just prior to inspection by microscope, and cell chamber depths of 12 μm, 20 μm and 50 μm were used during the experimentation.

Spermatozoa were observed using a microscope and a digital image capture system. This was based on a Nikon Eclipse E600 upright microscope fitted with phase contrast rings, an (x, y, z) motorized, heated stage and a × 20 objective (numerical aperture 0.45). At this magnification, the field of view was approximately 0.05 mm × 0.05 mm, and the depth of field was calculated to be 4 μm. Stage illumination was provided by a lamphouse fitted with a 100-W halogen bulb. For digital video photography, the microscope was equipped with a Dalsa model 2M30 monochrome, 10-bit digital video camera, which has a pixel resolution of 1600 × 1200 pixel and a sensor size of 7.4 μm per pixel. The normal framing rate of the camera was 30 Hz, but experiments were also performed with a framing rate of 121 Hz for which a smaller image area of 1600 × 200 pixel was recorded. Microscope stage position control and image capture were provided by a PC running Windows 2000XP programmed in Labview™. The camera interface to the computer was provided by a National Instruments PCI-1428 Camera Link™ image acquisition card, and the microscope stage position control signals were sent through an RS-232 interface. Camera exposure was set automatically such that the images were not saturated, and a typical exposure time was 1 ms. Image sequences were saved in uncompressed TIFF format. All image analysis, and indeed all hydrodynamic analysis, was performed on Apple G4 and G5 platforms running OS X.

A sequence of still images in figure 16 shows the typical raw image data. The centroid of the head was tracked automatically, as was head principal axis (orientation). Progressive motility was determined using standard parameters, including straight-line velocity *VSL*, average path velocity *VAP* and amplitude of

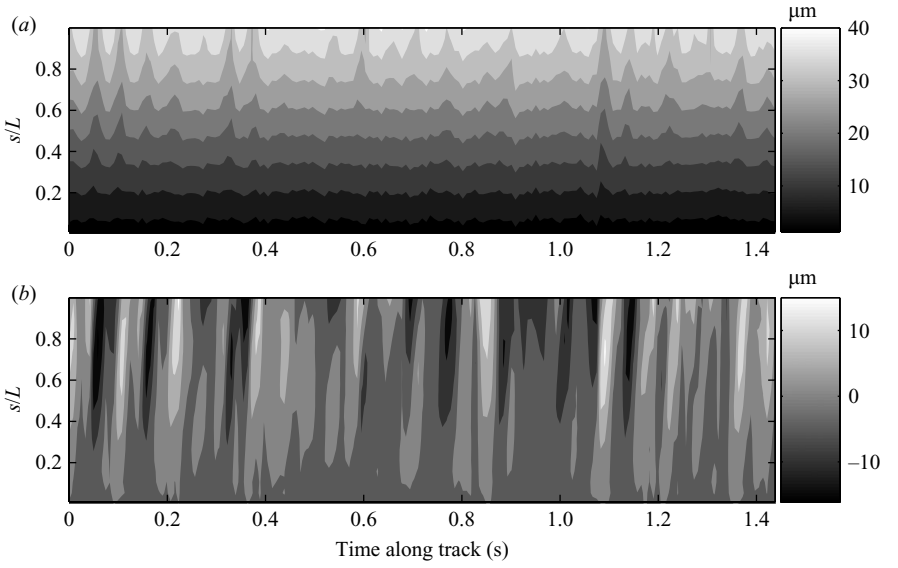

FIGURE 17. Contours of position coordinates for the flagellum of the sperm depicted in figure 16: (*a*) $x(s/L, t)$ coordinate; (*b*) $y(s/L, t)$ coordinate. This data is used to estimate the flagellar beat velocity.

lateral head movement *ALH* (Mortimer 1994). The average path is calculated, based on a 30 Hz data sample, with a 5-point moving average of the X–Y track positions. In all of our images, the flagellum could be discerned as a change in grey level, but sometimes the distal end of the flagellum was indistinct. The flagellum may not be clearly delineated in some images (mainly because of slight out-of-focal plane motion or position), but it is clear enough to determine the flagellum length L at some time points. As we assumed the flagellum to be inextensible (which is approximately correct Lighthill 1976), we then fixed the tail length in all of the images as L. The proximal end of the tail next to the head was distinct in each image, and a model flagellum was fitted to each image by the following procedure: from the start point an arc was drawn towards the distal end of the flagellum at radius ds (with ds approximately $L/100$), and a new point was placed at the position of maximum grey level on this arc. This new point corresponds to the flagellum position distance ds from the start point. The process is repeated for the second point, and so on until the flagellum model has a total length L. For some of the images, the unclear termination of the flagellum presented a difficulty. In these cases, the clear points on the flagellum were used to fit a fourth-order polynomial, which was then extrapolated to total length L. Raw manipulation of the images yielded tail lengths that varied ± 6 μm because of optically unclear regions at the distal end of the tail, or from out-of-focal plane movement, but this procedure rectified this length variation. Our image set (given the small depth of field and the fact that most of the flagellum maintained focus in each frame) indicated that these non-planar flagellum motions were quite small. For one of our experiments, this automatic tracking and morphology procedure was verified by additional manual tracing of the track and tail. A typical set of tail data, gathered automatically, is shown in figure 17. An example of a section of the automatically measured centroid track and propulsive velocities, associated with this flagellum data, is shown in figure 18. This figure shows results typical of forward progressive sperm,

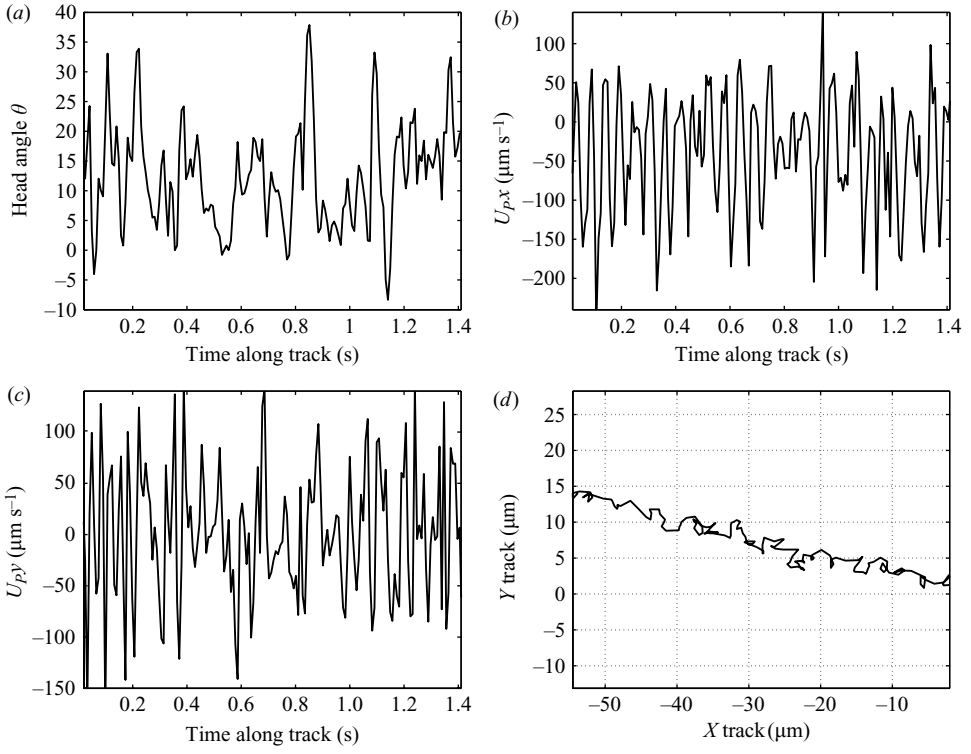

FIGURE 18. Typical graphs of kinematic parameters measured for the forward progressive sperm image sequence in figure 16 and flagellum data in figure 17: (*a*) head angle θ (deg), (*b*) local (head-aligned) frame propulsive velocity U_{px}, (*c*) local (head aligned) lateral velocity U_{py} (μm s^{-1}) and (*d*) head centroid track.

with a local U_{px} velocity biased in the forward direction (in this case $-x$) and a more or less zero average U_{py}. In the raw images, the sperm head was seen to rotate alternately (broadly about the x axis) and so presented an oscillating width profile to the microscope. Small variations in observed head length were also seen in the raw images, indicating that the head pitches out of the x–y plane slightly. These motions must result from undetected out-of-plane tail motion. Although the hydrodynamic simulation was three-dimensional, we could extract only two-dimensional (x–y plane) information from the camera and microscope. The simulation is therefore incapable of reproducing this observed head motion, and we were therefore intrigued as to how the experimentally recorded tracks would compare to the hydrodynamic simulations. As the head presented a time-varying profile to the camera, an averaging method was used to approximate head length and width. All of the sperm we measured had length and width close to the values published by Brennen & Winet (1977) of 5.8×3.1 μm and so, because of the difficulty in obtaining exact head dimensions, we chose this morphology as the standard head morphology for simulation.

REFERENCES

AINLEY, J., DURKIN, S., EMBID, R., BOINDALA, P. & CORTEZ, R. 2008 The method of images for regularized stokeslets. *J. Comput. Phys.* **227**, 4600–4616.

Aitken, R. J., Sutton, M., Warner, P. & Richardson, D. W. 1985 Relationship between the movement characteristics of human spermatozoa and their ability to penetrate cervical mucus and zona free hamster oocytes. *J. Reprod. Fertil.* **73**, 441–449.

Birkhead, T. 2000 *Promiscuity: An Evolutionary History of Sperm Competition and Sexual Conflict*. Faber & Faber.

Blake, J. R. 1971 Infinite models for ciliary propulsion. *J. Fluid Mech.* **49**, 209–222.

Blake, J. R. & Chwang, A. T. 1974 Fundamental singularities of viscous flow. Part 1. The image system in the vicinity of a stationary no-slip boundary. *J. Engng Math.* **8**, 23–29.

Brennen, C. & Winet, H. 1977 Fluid mechanics of propulsion by cilia and flagella. *Annu. Rev. Fluid Mech.* **9**, 339–398.

Brenner, H. 1962 The effects of finite boundaries on the stokes resistance of an arbitrary particle. *J. Fluid Mech.* **12**, 35–48.

Brokaw, C. J. 1970 Bending moments in free-swimming flagella. *J. Exp. Biol.* **43**, 155–169.

Cisneros, L. H., Cortez, R., Dombrowski, C., Goldstein, R. E. & Kessler, J. O. 2007 Fluid dynamics of self-propelled microorganisms, from individuals to concentrated populations. *Exper. Fluids* **43**, 737–753.

Cortez, R. 2001 The method of regularized stokeslets. *SIAM J. Sci. Comput.* **23** (4), 1204–1225.

Cortez, R., Fauci, L. & Medovikov, A. 2005 The method of regularized stokeslets in three dimensions: analysis, validation, and application to helical swimming. *Phys. Fluids* **17**.

Dresdner, R. D. & Katz, D. F. 1981 Relationships of mammalian sperm motility and morphology to hydrodynamic aspects of cell function. *Biol. Reprod.* **25**, 920–930.

Dresdner, R. D., Katz, D. F. & Berger, S. A. 1980 The propulsion by large amplitude waves of uniflagellar micro-organisms of finite length. *J. Fluid Mech.* **97**, 591–621.

Fauci, L. J. & Dillon, R. 2006 Biofluidmechanics of reproduction. *Annu. Rev. Fluid Mech.* **38**, 371–394.

Fulford, G. R. & Blake, J. R. 1983 On the motion of a slender body near an interface between two immiscible fluids at low Reynolds numbers. *J. Fluid Mech.* **127**, 203–217.

Gomendio, M., Malo, A. F., Garde, J. & Roldan, E. R. S. 2007 Sperm traits and male fertility in natural populations. *Reproduction* **134**, 19–29.

Gray, J. & Hancock, G. J. 1955 The propulsion of sea-urchin spermatozoa. *J. Exp. Biol.* **32**, 82–814.

Gueron, S. & Liron, N. 1992 Ciliary motion modelling, and dynamic multicilia interactions. *Biophysical J.* **63**, 1045–1058.

Hancock, G. J. 1953 The self-propulsion of microscopic organisms through liquids. *Proc. R. Soc. Lond.* A **217**, 96–121.

Happel, J. & Brenner, H. 1981 *Low Reynolds Number Hydrodynamics*, 2nd ed. Springer.

Higdon, J. J. L. 1979 A hydrodynamic analysis of flagellar propulsion. *J. Fluid Mech.* **90**, 685–711.

Ishikawa, T., Sekiya, G., Imai, Y. & Yamaguchi, T. 2007 Hydrodynamic interactions between two swimming bacteria. *Biophys. J.* **93**, 2217–2225.

Johnson, R. E. & Brokaw, C. J. 1979 Flagellar hydrodynamics: a comparison between resistive-force theory and slender-body theory. *Biophys. J.* **25**, 113–127.

Katz, D. F. 1974 On the propulsion of micro-organisms near solid boundaries. *J. Fluid Mech.* **64**, 33–49.

Kim, S. & Karilla, J. S. 1991 *Microhydrodynamics: Principles and Selected Applications*. Butterworth Heinemann.

Larsen, L., Scheike, T., Jensen, T. K., Bonde, J. P., Ernst, E., Hjollund, N. H., Zhou, Y., Skakkebaek, N. E. & Giwercman, A. 2000 Computer-assisted semen analysis parameters as predictors for fertility of men from the general population. *Hum. Reprod.* **15**, 1562–1567.

Lighthill, J. 1976 Flagellar hydrodynamics: the John von Neumann lecture. *SIAM Review* **18**, 161–229.

Mortimer, D. 1994 Practical laboratory andrology, chapter 7. In *Computer-Aided Sperm Analysis*. Oxford University Press.

Owen, D. H. & Katz, D. F. 2005 A review of the physical and chemical properties of human semen and the formulation of a semen simulant. *J. Androl.* **26** (4), 459–469.

Phan-Thien, N., Tran-Cong, T. & Ramia, M 1987 A boundary-element analysis of flagellar propulsion. *J. Fluid Mech.* **184**, 533–549.

Ramia, M., Tullock, D. L. & Phan-Thien, N. 1993 The role of hydrodynamic interaction in the locomotion of microorganisms. *Biophys. J.* **65**, 755–778.

Reynolds, A. J. 1965 The swimming of minute organisms. *J. Fluid Mech.* **23**, 241–260.

Rothschild, Lord 1963 Non-random distribution of bull spermatozoa in a drop of sperm suspension. *Nature* **198**, 1221.

Suarez, S. S. & Pacey, A. A. 2006 Sperm transport in the female reproductive tract. *Hum. Reprod. Update* **20**, 23–37.

Taylor, G. I. 1951 Analysis of the swimming of microscopic organisms. *Proc. R. Soc. Lond.* A **209**, 447–461.

WHO 1999 *WHO Laboratory Manual for the Examination of Human Semen and Sperm–Cervical Mucus Interaction*, 4th ed. Cambridge University Press.

Yundt, A. P., Shack, W. J. & Lardner, T. J. 1975 Applicability of hydrodynamic analyses of spermatozoan motion. *J. Exp. Biol.* **62**, 27–41.